Check for updates

Small

NANO · MICRO small
www.small-journal.com

RESEARCH ARTICLE

Ultrathin Magnesium-Ion Selective COF Membranes for Efficient Osmotic Power and Iontronic Logic Control

Lixue Yang[1,2] | Yixin Xu[3] | Yan Du[1,4] | Feiyao Yang[1] | Yanguang Zhou[3] | Zhe Wang[2,5,6] | Zhong Lin Wang[1] | Di Wei[1,7]

[1]Beijing Institute of Nanoenergy and Nanosystems, Chinese Academy of Sciences, Beijing, P. R. China | [2]School of Chemistry and Life Sciences, Changchun University of Technology, Changchun, P. R. China | [3]Department of Mechanical and Aerospace Engineering, The Hong Kong University of Science and Technology, Kowloon, Hong Kong | [4]School of Nanoscience and Engineering, University of Chinese Academy of Sciences, Beijing, P. R. China | [5]Advanced Institute of Materials Science, Changchun University of Technology, Changchun, P. R. China | [6]Key Laboratory of Advanced Functional Polymer Membrane Materials of Jilin Province, Changchun, P. R. China | [7]Centre for Photonic Devices and Sensors, University of Cambridge, Cambridge, UK

Correspondence: Yanguang Zhou (maeygzhou@ust.hk) | Zhe Wang (wangzhe@ccut.edu.cn) | Zhong Lin Wang (zlwang@binn.cas.cn) | Di Wei (weidi@binn.cas.cn)

Received: 8 May 2026 | **Revised:** 13 May 2026 | **Accepted:** 3 June 2026

Keywords: covalent organic framework (COF) membranes | iontronic logic control | Mg^{2+} selective transport | osmotic power conversion

ABSTRACT

Magnesium ions (Mg^{2+}), vital for biological signaling and energy regulation, remain challenging to selectively and efficiently transport using artificial membranes, which typically lack molecular recognition and confined ion channels. Here, we report a β-ketoenamine covalent organic framework (TAPA-TFP COF) membrane that achieves near-ideal Mg^{2+} selectivity ($t_+ = 0.98$) and ultrafast transport through ordered 13.6 Å nanochannels. Structural and molecular dynamics analyses reveal that the precisely arranged O/N coordination sites within the porous nanochannels partially strip the Mg^{2+} hydration shell, while C = O···H—O—H hydrogen-bond networks lower migration barriers, enabling high permeability. The ultrathin, large-area, and defect-free membrane delivers record osmotic power and current densities of 636.64 W m^{-2} and 9213.3 A m^{-2} under a 500-fold salinity gradient. Beyond efficient power generation, the Mg^{2+}-selective nanochannels enable iontronic transistors, logic operations, and multimodal signal transduction, establishing a molecularly engineered porous platform that integrates ion-specific transport with energy conversion and information processing.

1 | Introduction

Ion transport underpins numerous processes of information transmission and energy conversion within living organisms, a phenomenon prevalent throughout nature [1–4]. Typically, multiple ions exist within biological systems, each conveying distinct forms of energy and information via salinity gradients, thereby achieving permeation coupling between energy and information. In recent years, there have been significant interest in developing artificial biological channels, because of their promising applications in water treatment [5], nanofluidic devices [6], ion gating [7] and beyond. Numerous artificial ion channels/membranes have been designed to achieve energy-information permeation coupling [8]. Yet realizing true energy-information coupling in artificial ion channels requires membranes that are simultaneously highly selective, ultrathin, a combination that remains exceptionally difficult to achieve. In ion-selective energy materials, this translates into a central design imperative where pore

Lixue Yang and Yixin Xu contributed equally to this work.

© 2026 Wiley-VCH GmbH

architectures must be engineered with molecular precision to govern ion transport within a confined volume. Accordingly, the goal is not only to maximise ion-mediated energy conversion, but also to endow transport with programmable selectivity and directionality, providing the physical basis for iontronic logic control. Accordingly, task-specific porous structures are required in which pore geometry and chemistry are deliberately tailored to enable efficient magnesium ions (Mg^{2+}) conduction while suppressing competing pathways and parasitic processes.

Research on artificial ion channels has advanced most rapidly in the area of biomimetic proton conduction, where transport mechanisms are now relatively well understood. Among these, the Grotthuss mechanism [9], characterized by ultrafast proton hopping along hydrogen-bonded networks, has been identified as a dominant pathway. For example, biomimetic two-dimensional (2D) crown-ether-based polyimide membranes could assemble highly ordered hydrogen-bonded water channels that created uninterrupted proton-conduction pathways, resulting in exceptional transport efficiency [10]. In contrast, artificial channels designed for divalent ions remain far less developed, despite their greater potential for energy and information transfer, ions such as magnesium ions (Mg^{2+}) inherently carry twice the charge of monovalent species, enabling higher signal density and energy throughput per transported ion. Mg^{2+} ions, in particular, are indispensable for enzymatic catalysis, nucleic acid stabilization, and intracellular signaling regulation. Several strategies have been developed to enhance Mg^{2+} transport [11]. For instance, bio-inspired mixed ion-electron conducting interphases employed polymer alloy hybrid architectures that integrated rapid ion channels within the polymer matrix and Mg^{2+} affinitive sites within the alloy layer. This design lowered nucleation barriers, promoted uniform deposition, and drastically enhanced rate capability, enabling stable cycling at record-high current densities of up to 6 mA cm^{-2} [12]. Mimicking the allosteric regulation of biological channels such as Magnesium transporter E (MgtE) further enabled intelligent control over Mg^{2+} transport [13]. In parallel, defect-engineering strategies, particularly the introduction of oxygen vacancies, significantly boosted Mg^{2+} conductivity by disrupting coordination shells and facilitating surface migration [14]. Structural modification through Mg^{2+} doping could also generate cation vacancies, optimize migration pathways, accelerate directional Mg^{2+} transport, and reduce diffusion energy barriers [15]. Nevertheless, studies targeting selective Mg^{2+} transport through synthetic membranes are still scarce, and the underlying transport mechanisms remain largely unexplored. This imbalance underscores a critical opportunity: achieving artificial channels that combine Mg^{2+} selectivity with rapid transport could enable high density energy-information coupling at the molecular scale. Advancing this direction will require the development of ultrathin, structurally tailored membrane architectures that can mediate dehydration, coordination, and migration of divalent ions with both precision and efficiency.

Covalent organic frameworks (COFs) provide a highly promising platform for achieving ion-selective transport and fabricating ultrathin membranes, representing an ideal class of porous crystalline materials for this purpose, owing to their ordered porous channels, molecularly tunable architectures, and excellent chemical stability [16–19]. Recently, substantial progress has been made in COF-based membranes for precise ion separation. For example, Wang et al. developed a 430–450 nm thick carbon-organic framework membrane featuring localized ion-trapping sites, which delivered an impressive Li^+/Mg^{2+} selectivity of 190 [20]. In another study, a biomimetic nanocomposite membrane was constructed by integrating 2D sulfonated COF nanosheets with anion-grafted aramid nanofibers (ANF), yielding high performance osmotic power conversion. With a thickness of 7.2 μm, this membrane achieved a Na^+ transference number of 0.86 and a power density of 62.9 W m^{-2} under a 500-fold salinity gradient [21]. Sun et al. developed β-ketoenamine-linked COF membranes via de novo encapsulation of Na^+-selective ionophores, realizing remarkable Na^+/K^+ and Na^+/Li^+ selectivity for enhanced osmotic energy harvesting [22]. Another work introduced aligned dipolar benzothiadiazole moieties into 1D COF nanochannels, enabling dynamically switchable permselectivity between cation- and anion-selective transport through ion-dipole interactions [23]. Furthermore, Sun's group demonstrated that linkage engineering modulates short-range ion–framework interactions, affording COF membranes with record-high permselectivity even under high-salinity conditions for thermoelectric energy conversion [24]. Despite these impressive advances, most COF membranes are designed for monovalent ion selectivity; strategies for efficient and selective Mg^{2+} transport toward osmotic power and iontronics remain scarce.

In conventional nanoconfined channels, Mg^{2+} ions selectivity was typically achieved by blocking its transport rather than facilitating it. Common strategies include precise size-based sieving, in which pores were designed slightly smaller than the hydrated radius of Mg^{2+} but larger than that of monovalent ions, as well as electrostatic interactions and the Donnan effect, all of which generate strong repulsion against divalent cations [25, 26]. Additional mechanisms, such as counterion accumulation and dual confinement of ions and pores, can trap Mg^{2+} near functional groups on the pore walls, leaving central pathways accessible for monovalent ion transport [25, 27]. Although these synergistic mechanisms effectively enhance selectivity for monovalent ions, they inherently restrict Mg^{2+} permeation and limit the flux of divalent ions. This limitation stems from the absence of synergistic interplay between nanoconfined channels and ion-specific binding sites, as well as the lack of functional groups capable of coordinating Mg^{2+} while excluding competing cations. The transport of magnesium ions are inherently hindered by their high charge density and strongly bound hydration shell [28], requiring them to overcome substantial dehydration energy barriers. Consequently, conventional membrane materials struggle to achieve both high selectivity and high transport efficiency for Mg^{2+}. Overcoming these challenges demands precise molecular engineering and nanoscale confinement to modulate ion coordination, dehydration, and migration. In this context, β-ketoenamine linkages emerge as promising Mg^{2+}-conducting motifs [29, 30]: C = O group and H_2O can form hydrogen-bonded networks that facilitate dehydration and guide ion transport. Incorporating β-ketoenamine units into COF nanochannels therefore offer a viable strategy to enable selective and efficient Mg^{2+} conduction. This work pioneers a design framework that couples structural confinement with molecular-level recognition, providing a pathway toward next-generation materials for osmotic power conversion and iontronic applications.

16136829, 2026, 44, Downloaded from https://onlinelibrary.wiley.com/doi/10.1002/smll.74164 by Cas-Beijing Institution Of, Wiley Online Library on [09/08/2026]. See the Terms and Conditions (https://onlinelibrary.wiley.com/terms-and-conditions) on Wiley Online Library for rules of use; OA articles are governed by the applicable Creative Commons License

Here, we reported ultrathin β-ketoenamine COF membranes, synthesized via room-temperature interfacial polymerization of tri (4-aminophenyl) amine (TAPA) and 2,4,6-triformylresorcinol (TFP) under acetic acid catalysis, that exhibited exceptional Mg^{2+} selectivity. By assembling molecular building blocks, we first realized highly efficient and selective Mg^{2+} transport. This strategy enabled the fabrication of large-area, free-standing, and defect-free COF films with a thickness of 250 nm. Remarkably, the membranes retained mechanical integrity and flexibility even after drying, indicating robust structural stability. Both experimental characterization and molecular simulations confirmed that the β-ketoenamine linkages generated highly specific coordination environments for Mg^{2+}. Within these frameworks, hydrogen-bonded networks between H_2O and C = O groups facilitated partial dehydration and reduced migration energy barriers, collectively promoting divalent ion transport over monovalent competitors. As a result, the TAPA-TFP COF membrane achieved a Mg^{2+} selectivity of 0.98, approaching the ideal value of 1, and substantially outperformed other cations such as K^+, Na^+, Li^+, and Ca^{2+}. When integrated into an osmotic power conversion system, the membrane delivered an ultrahigh power density of 636.64 W m^{-2} under a 500-fold salinity gradient, surpassing previously reported osmotic membranes. Beyond power generation, the Mg^{2+} selective channels enabled iontronic logic control driven solely by salinity gradients, eliminating the need for external gate voltages. By leveraging ion-specific signals generated through multi-ion transport, the iontronic transistor achieved gate-free modulation of ionic flux, establishing a new paradigm for ultra-low-power logic operation. This mechanism further enabled programmable actuation in soft robotic systems and reshaped the design principles of ion-based logic architectures, offering a promising foundation for next-generation human–machine interfaces and adaptive iontronic devices. Moreover, this work provides not only a route for constructing ultrathin, free-standing COF membranes with selective ion channels, but also a materials blueprint for next-generation osmotic power converters, iontronic logic strcutures, and bioinspired systems that couple energy transduction with information processing through divalent ions transport.

2 | Results

2.1 | Preparation and Characterization of COF Membranes

A room-temperature Schiff-base interfacial polymerization (IP) strategy was employed to fabricate large-area, free-standing COF films [31]. Figures S1–S3 summarized the experimental steps and trial outcomes explored during the optimization of fabrication parameters, while Figure 1a presented the finalized protocol for COF films preparation. Tris (4-aminophenyl) amine (TAPA) and 2,4,6-triformylphloroglucinol (TFP) were first dissolved in dichloromethane (DCM) to form the organic phase. The solution was then left undisturbed for 1 h to allow the formation of a stable organic interface. Subsequently, an aqueous phase was carefully introduced above the organic layer, followed by the gentle addition of acetic acid as a catalyst into the aqueous phase. The 1 h pre-equilibration step prior to initiating the reaction proved essential for obtaining continuous, transparent, and self-supporting COF films. This process promoted uniform monomer distribution within the organic phase and minimized local concentration gradients at the interface during the early stages of polymerization. Consequently, defect formation was suppressed, enabling the ambient fabrication of stable, homogeneous TAPA-TFP COF films featuring β-ketoenamine linkages. Using the same IP strategy, TAPA-1,3,5-triformylbenzene (TFB) membranes linked exclusively through imine (C═N) bonds were also fabricated (Figure S4). This structural difference led to marked variations in pore architecture, surface chemistry, and ion transport behavior compared to the β-ketoenamine-linked TAPA-TFP membranes. Both membrane types exhibited favorable hydrophilicity, which not only facilitated their detachment from the aqueous phase but also supported subsequent ion transport characterization (Figure S5). Figure 1b and Figure S6 showed the chemical structures of TAPA-TFP and TAPA-TFB COF films from the optimal IP procedure. Owing to the self-sealing and self-limiting characteristics inherent of IP, the TAPA-TFP films further displayed excellent mechanical robustness. As shown in Videos S1 and S2, the β-ketoenamine-linked TAPA-TFP membrane withstood repeated stretching and tearing without any visible damage, retaining both flexibility and structural integrity even after drying, strongly confirming its mechanical robustness. In contrast, the imine-linked TAPA-TFB membrane fractured easily under the same conditions, highlighting its inferior mechanical strength (Video S3). This pronounced difference originated from the distinct bonding chemistries of the two frameworks [32]. In TAPA-TFP, β-ketoenamine linkages underwent irreversible tautomerization to form a fully conjugated backbone. This bonding mode enhanced crystallinity, minimized defect formation, and strengthened interlayer π–π interactions, collectively reinforcing mechanical stability. By comparison, the imine bonds in TAPA-TFB were reversible and less conjugated, which promoted defect generation and weakened interlayer interactions, ultimately leading to inadequate mechanical performance.

To elucidate the internal structure, the surface morphology, cross-section, and thickness of the membranes were examined via field-emission scanning electron microscopy (FESEM) and atomic force microscopy (AFM). As shown in Figure 1c and Figure S7, both COF films exhibited exceptionally smooth and uniform surfaces, free of polymer agglomerations or visible defects. Energy-dispersive spectroscopy (EDS) confirmed homogeneous distributions of carbon and nitrogen in TAPA-TFP and TAPA-TFB films, whereas oxygen was prominently detected only in TAPA-TFP, consistent with their respective chemical compositions (Figures S8 and S9). Cross-sectional FESEM images and AFM measurements indicated that the self-standing COF films possessed a uniform thickness of ~250 nm (Figure 1d–f and Figures S10 and S11). The chemical structures of the COF membranes were characterized by Fourier-transform infrared spectroscopy (FTIR) and X-ray photoelectron spectroscopy (XPS) [33]. For the TAPA-TFP film, the amine N-H stretching vibration band (3100–3300 cm^{-1})) was completely absent, while a new C-N stretching peak appeared at 1256 cm^{-1}) (Figure 1g). The C═O stretching band broadened and red-shifted to 1615 cm^{-1}, merging with the C═C stretching signal at 1560 cm^{-1}, indicative of β-ketoenamine formation and extensive intraframework hydrogen bonding (Figure 1g). In contrast, the TAPA-TFB film exhibited a distinct C═N imine peak at 1265 cm^{-1} (Figure 1g). XPS analysis further corroborated these findings. As depicted in Figure 1h, TAPA-TFB comprised solely carbon and nitrogen, whereas

16136829, 2026, 44, Downloaded from https://onlinelibrary.wiley.com/doi/10.1002/smll.74164 by Cas-Beijing Institution Of, Wiley Online Library on [09/08/2026]. See the Terms and Conditions (https://onlinelibrary.wiley.com/terms-and-conditions) on Wiley Online Library for rules of use; OA articles are governed by the applicable Creative Commons License

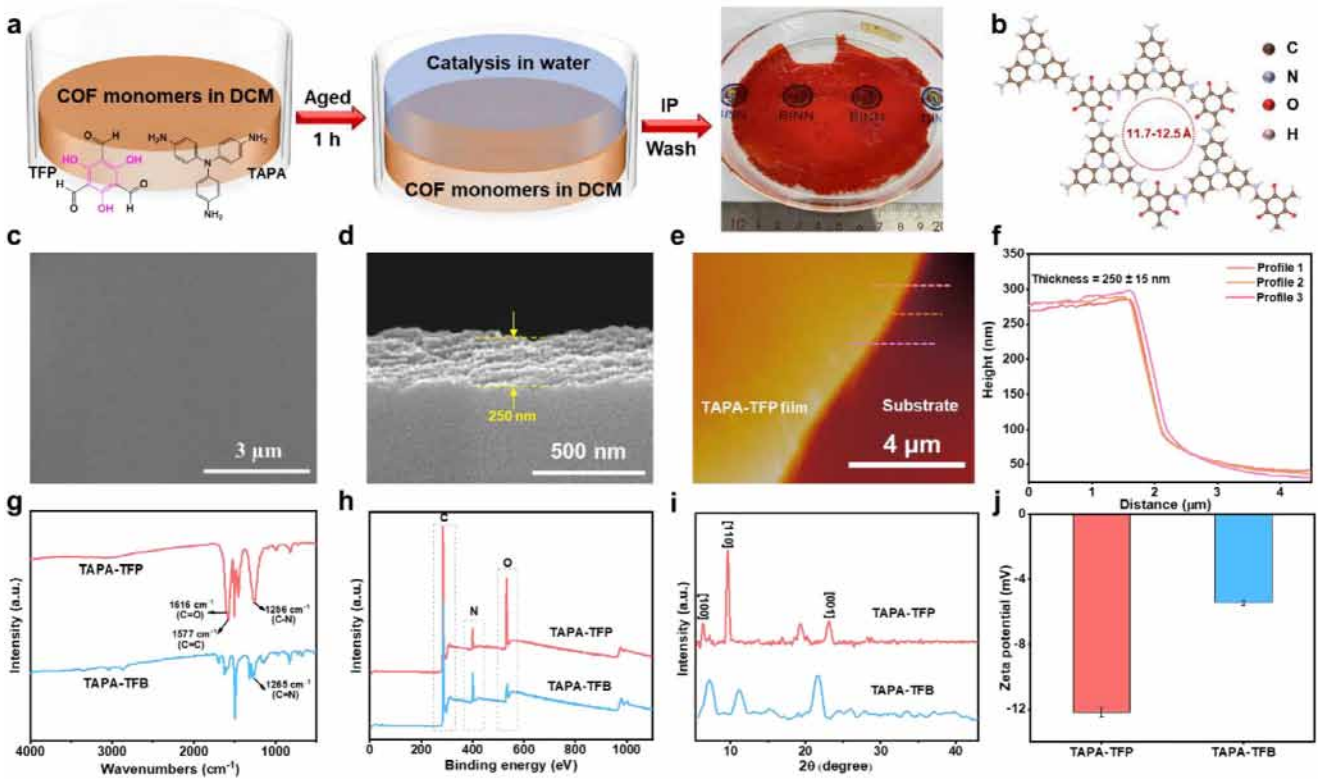


FIGURE 1 | Synthesis and characterization of TAPA-TFP COF membranes. (a) Schematic illustration and photograph of the optimal interfacial polymerization (IP) process for fabricating TAPA-TFP COF membranes. (b) Chemical structure of the TAPA-TFP membrane, where brown, light blue, red spheres, and gray spheres represent C, N, O, and H atoms, respectively. (c) Surface SEM image of the TAPA-TFP COF membrane. (d) Cross-sectional SEM image of the TAPA-TFP COF membrane. (e), (f) AFM images showing the surface morphology and thickness of the TAPA-TFP COF membrane. (g) FTIR spectra of TAPA-TFP and TAPA-TFB COF membranes. (h) XPS spectra of TAPA-TFP and TAPA-TFB COF membranes. (i) XRD patterns of TAPA-TFP and TAPA-TFB COF membranes. (j) Zeta potentials of TAPA-TFP and TAPA-TFB COF membranes in deionized water.

TAPA-TFP contained additional oxygen species. The C 1s spectra of both COF membranes retained their characteristic profiles without significant energy shifts, exhibiting three distinct peaks within the binding energy range of 284.2 to 286.8 eV (Figures S12a and S13a). In contrast, the high-resolution N 1s spectrum of TAPA-TFB displayed two distinct peaks at 399.3 eV and 400.9 eV, corresponding to nitrogen species from C═N—C and C═N—H bonds respectively (Figure S12b). In TAPA-TFP, the introduction of a hydroxyl group and subsequent enol-ketone tautomerization shifted the 400.9 eV imine nitrogen peak to 399.5 eV, characteristic of nitrogen in the β-ketoenamine moiety (Figure S13b). Concurrently, the O 1s spectrum of TAPA-TFP exhibited a new peak at 531.2 eV, corresponding to oxygen in the β-ketoenamine moiety (Figure S13c). Collectively, these results confirmed the successful synthesis of the designed COFs.

X-ray diffraction (XRD) analysis was performed to investigate the ordered structures of the COF membranes. As shown in Figure 1i, the TAPA-TFP film exhibited a sharp diffraction peak at a relatively low $2\theta \approx 6.37°$, which was assigned to the reflection from the (100) plane with an aperture of approximately 13.6 Å. The pore size evaluated from XRD results match well with the predicted aperture sizes of TAPA-TFP (11.7 to 12.5 Å) films [34] shown in Figure 1b. The final broad peak at the maximum 2θ angle of 22.4° was attributed to the (001) crystal plane arising from π–π stacking between successive COF layers, with a spacing of 3.9 Å. The (100) peak of the TAPA-TFB film shifted to a slightly higher 2θ value of 7.1°, indicating a slightly smaller pore size of approximately 12.5 Å, the pore size derived from the XRD results is consistent with the theoretical aperture range of TAPA-TFB films (12.4 to13.7 Å) [34] presented in Figure S5. Meanwhile, the (001) peak appearing at $2\theta \approx 21.67°$, corresponding to an interlayer spacing of approximately 4.0 Å. These values were highly consistent with the pore size range reported in the literature [34]. Notably, a marked difference in XRD peak intensity was observed between the two COF films. The diffraction peaks of TAPA-TFP were sharper, reflecting higher crystallinity, whereas those of TAPA-TFB were comparatively weaker. Typically, the enhanced crystallinity of TAPA-TFP can be attributed to the introduction of β-ketoenamine bonds, which promote the formation of a stable hydrogen-bond network, thereby improving the framework's order and structural stability. Zeta potential measurements revealed a zeta potential of −5.45 mV for the TAPA-TFB membrane, while the TAPA-TFP membrane exhibited a higher negative charge with a zeta potential of −12.2 mV, approximately 2.5 times that of TAPA-TFB (Figure 1j).

2.2 | Ion Selectivity and Permeability of COF Membranes

To evaluate the ion selectivity and permeability of COF membranes, we systematically investigated their ion transport behavior in a two-compartment electrolytic cell. Following

16136829, 2026, 44, Downloaded from https://onlinelibrary.wiley.com/doi/10.1002/smll.74164 by Cas-Beijing Institution Of, Wiley Online Library on [09/08/2026]. See the Terms and Conditions (https://onlinelibrary.wiley.com/terms-and-conditions) on Wiley Online Library for rules of use; OA articles are governed by the applicable Creative Commons License

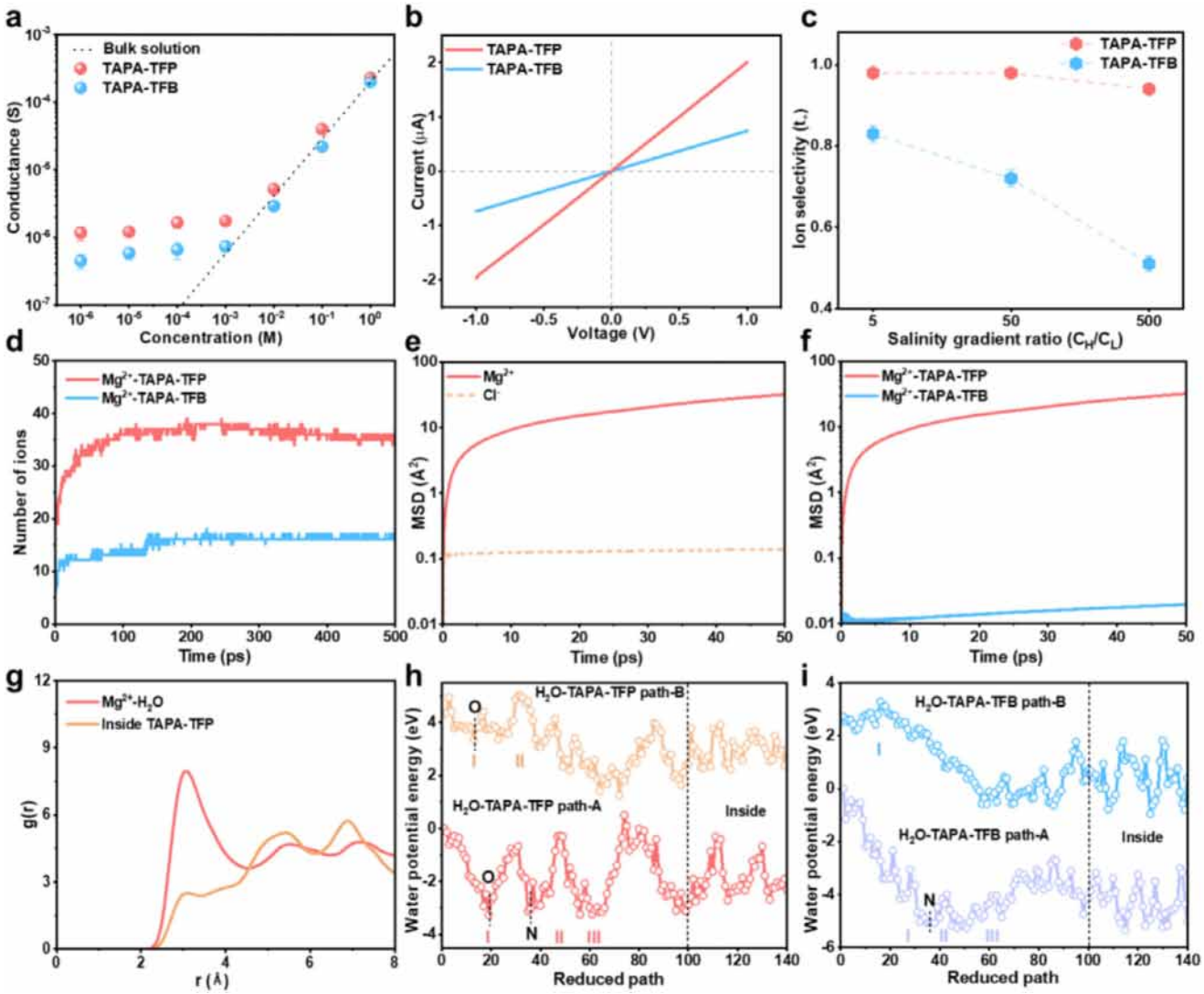


FIGURE 2 | The ion selectivity and ion transport mechanism of the COF membranes. (a) Ionic conductances of TAPA-TFP and TAPA-TFB membranes measured in KCl electrolytes with concentrations ranging from 10^{-6} to 1 M. Dots represent experimental data, and dashed lines denote bulk-solution fits. (b) Current-voltage (*I–V*) curves of TAPA-TFP and TAPA-TFB membranes in 0.001 M $MgCl_2$. (c) Cation transference numbers (t_+) of TAPA-TFP and TAPA-TFB membranes under $MgCl_2$ salinity gradients of 0.05 M/0.01 M, 0.5 M/0.01 M, and 5 M/0.01 M $MgCl_2$. (d) Temporal evolution of Mg^{2+} translocation events through TAPA-TFP and TAPA-TFB membranes. (e) Mean square displacement (MSD) of Mg^{2+} and Cl^- ions across TAPA-TFP membranes as a function of time. (f) MSD comparison of Mg^{2+} transport through TAPA-TFP and TAPA-TFB membranes. (g) Radial distribution functions (RDFs) of Mg^{2+}-H_2O around TAPA-TFP nanopores (pink) and of Mg^{2+} ions entering the pores (yellow). (h) Water potential energy for H_2O migration through the TAPA-TFP membrane along pathway A (pink) and pathway B (yellow). (i) Water potential energy for H_2O migration through the TAPA-TFB membrane along pathway A (light purple) and pathway B (blue).

performance analysis, the optimal TAPA-TFP membrane was selected for subsequent experiments. The ion transport property of the TAPA-TFP membrane was first explored based on a KCl system due to the similar bulk mobility and hydration radii of K^+ and Cl^- ions [35, 36]. The interference of redox potential was eliminated using Ag/AgCl electrodes with agar-saturated KCl salt bridges [37]. As anticipated, both membranes exhibited linear ohmic behavior, indicating effective ion transport across the membrane (Figure S14) [38]. The ion conductance values of TAPA-TFP and TAPA-TFB membranes remained nearly constant in the low-concentration region, signifying surface charge-controlled ion transport (Figure 2a). Figure 2b showed the current–voltage (*I–V*) curves measured when both reservoirs were filled with 0.001 M $MgCl_2$ solution. Surprisingly, the ion conductance of the TAPA-TFP membrane could be determined from the *I–V* curve (pink line) to be 2 μS, approximately 2.8 times higher than that of TAPA-TFB membranes. This substantial enhancement in Mg^{2+} transport was attributed to the fact that the β-ketoenamine structural units of TAPA-TFP channel could act as a binding site for Mg^{2+}, reducing migration energy barriers, thereby facilitating the transport of Mg^{2+}. Zeta potential confirmed the negatively charged surface on the TAPA-TFP membrane, indicating cation selectivity.

To quantitatively investigate the ion transport characteristics of TAPA-TFP membranes, we conducted *I–V* measurements using an asymmetric $MgCl_2$ solution, with a lower salinity concentration (C_L) set at 0.01 M and a higher salinity concentration

16136829, 2026, 44, Downloaded from https://onlinelibrary.wiley.com/doi/10.1002/smll.74164 by Cas-Beijing Institution Of, Wiley Online Library on [09/08/2026]. See the Terms and Conditions (https://onlinelibrary.wiley.com/terms-and-conditions) on Wiley Online Library for rules of use; OA articles are governed by the applicable Creative Commons License

(C_H) set at 0.5 M (Figure S15). The osmotic potential (V_{OS}) at zero current (open-circuit voltage) and the osmotic current (I_{SC}) at zero voltage (short-circuit current) were determined by identifying the intercepts of the *I–V* curves across a 50-fold $MgCl_2$ salinity gradient. As shown in Figure S16, the V_{OS} values for both TAPA-TFP and TAPA-TFB membranes were found to be proportional to the salinity gradient. Notably, the Vos of the TAPA-TFP membrane (48 mV) was markedly higher than that of TAPA-TFB (20 mV) under a 50-fold $MgCl_2$ salinity gradient (Figure S17). In this study, Mg^{2+} selectivity was assessed by the ion transference number (t_+) of the TAPA-TFP membrane [39]. As shown in Figure 2c and Figure S18, the t_+ values of both TAPA-TFP and TAPA-TFB membranes exhibited an inverse relationship with the salinity gradient. This behavior might stem from a reduction in the Debye length on the high-concentration side, thereby diminishing the ion selectivity of the COF membrane [40]. Notably, under a 50-fold $MgCl_2$ salinity gradient, the calculated t_+ value for the TAPA-TFP membrane reached 0.98, indicating strong cation selectivity approaching the ideal cation value of 1. Compared with TAPA-TFB (Figures S19 and S20), the enhanced cation selectivity and rapid ion transport observed in the *β*-ketoenamine TAPA-TFP COF channels contribute to the higher V_{OS} and t_+. To validate the strong Mg^{2+} selectivity of the TAPA-TFP membrane, we compared the transport behavior of other cations (K^+, Na^+, Li^+, and Ca^{2+}). Compared to other cations (K^+, Na^+, Li^+, and Ca^{2+}), the TAPA-TFP membrane exhibited significantly higher selectivity for Mg^{2+}, demonstrating unique and highly efficient magnesium ion transport capability (Figure S21). Consequently, the superior cation selectivity and ion permeability of the TAPA-TFP arose from a synergistic interplay of electrostatics, coordination interactions, hydrogen bonding, and pore architecture.

2.3 | Ion Selectivity Mechanism of the TAPA-TFP Membrane

To investigate the ion-selective transport behavior of the TAPA-TFP and TAPA-TFB membranes under salinity gradients, molecular dynamics (MD) simulations were conducted. First, the temporal variation of ion migration through the nanoscale channels was analyzed (Figures S22–S24 and Videos S4 and S5). The results showed that Mg^{2+} can readily pass through the COF channels, whereas Cl^- hardly permeated, indicating a pronounced cation selectivity of the COF channels. Moreover, under the same $MgCl_2$ salinity gradient, the number of Mg^{2+} ions passing through the TAPA-TFP nanoscale channels is significantly higher than that through TAPA-TFB, demonstrating that the TAPA-TFP membrane exhibits superior Mg^{2+} selectivity compared to TAPA-TFB (Figure 2d).

To characterize the dynamics of Mg^{2+} within the nanoscale channels, we calculated its mean square displacement (MSD) to evaluate the diffusion rate of Mg^{2+} in both TAPA-TFP and TAPA-TFB nanochannels. As shown in Figure 2e and Figure S25, the diffusion rates of Mg^{2+} in the TAPA-TFP and TAPA-TFB nanochannels were significantly higher than that of Cl^- ions, indicating that Mg^{2+} diffused much faster in the TAPA-TFP nanochannel, while the diffusion of Cl^- was strongly restricted. Meanwhile, under the same $MgCl_2$ salinity gradient, the diffusion rate of Mg^{2+} in the TAPA-TFP nanochannel was much higher than that in TAPA-TFB (Figure 2f), suggesting that Mg^{2+} migrated more rapidly and efficiently within the TAPA-TFP nanochannels. These results further confirmed the higher Mg^{2+} selectivity of the TAPA-TFP membrane, which was attributed to its larger pore size (13.6 Å) and the abundance of O/N coordination sites within the framework. Moreover, the C═O···H—O—H hydrogen-bond networks helped reduce migration resistance, allowing Mg^{2+} to partially dehydrate and pass through the channels smoothly. Further simulations of Ca^{2+} and K^+ diffusion in the TAPA-TFP nanochannel (Figure S26) revealed that their diffusion rates were markedly lower than that of Mg^{2+}, further demonstrating the high Mg^{2+} selectivity of the TAPA-TFP membrane. Furthermore, we computed the radial distribution function (RDF) of hydrated Mg^{2+} ions within TAPA-TFP and TAPA-TFB nanochannels. As shown in Figure 2g, the first peak of Mg^{2+}-H_2O pairs distribution largely decays as hydrated Mg^{2+} entered the TAPA-TFP nanopores, indicating a strong dehydration of the hydrated Mg^{2+}. In contrast, the degree of dehydration in the TAPA-TFB channels was notably weaker or even absent (Figure S27). It was noted that dehydration occurs as hydrated Mg^{2+} ions coordinate with the O/N sites on the exposed surface of TAPA-TFP. This partial stripping of the hydration shell enabled the Mg^{2+} ions to pass through the confined nanochannels.

To further understand the dehydration of Mg^{2+} ions within TAPA-TFP and TAPA-TFB nanopores, we simulated two characteristic transport pathways (A and B shown in Figures S28 and S29 and Videos S6 and S7) for water molecules on the COF surfaces. As shown in Figure 2h, water molecules traversing the TAPA-TFP surface became trapped at specific O and N sites, forming hydrogen bonds with the *β*-ketoenamine structure. These multiple hydrogen bonds established many high energy barriers for water diffusion (e.g., ~2.66 and ~2.85 eV). Consequently, the hydration shell of Mg^{2+} ions was readily destabilized as water molecules are drawn to these open O/N coordination sites. In the meanwhile, we showed that Mg^{2+} ions themselves can cross these O/N sites with a significantly lower energy activation (0.08 eV, Figure S30). The high density of these O/N sites on the TAPA-TFP surface thus collectively disrupted the hydration shell, enabling efficient cation migration. However, TAPA-TFB possessed fewer effective binding sites (limited to N atoms) and failed to establish a significant energy barrier for water diffusion. For instance, energy barriers hindering water migration were both fewer in number and significantly lower in magnitude on the TAPA-TFB surface when compared to TAPA-TFP. (Figure 2h,i). Consequently, water molecules remain coordinated with Mg^{2+} ions during transport across the TAPA-TFB surface, resulting in limited dehydration and a markedly reduced Mg^{2+} transport rate. This was further supported by MSD and potential energy surface calculations for water molecules on both COF surfaces (Figures S31 and S32). Our results confirmed a substantially higher energy barrier for water diffusion on the TAPA-TFP framework compared to TAPA-TFB, directly correlating with their distinct dehydration capabilities. Moreover, the slightly larger pore size of TAPA-TFP further reduced the energy barrier for Mg^{2+} passage through the channels, facilitating more efficient ion transport and enhancing the Mg^{2+} selectivity and permeability of the TAPA-TFP membrane.

The energy barrier curves of Mg^{2+}, K^+, and Ca^{2+} transport along the path-A inside the TAPA-TFP nanochannel are presented in

16136829, 2026, 44, Downloaded from https://onlinelibrary.wiley.com/doi/10.1002/smll.74164 by Cas-Beijing Institution Of, Wiley Online Library on [09/08/2026]. See the Terms and Conditions (https://onlinelibrary.wiley.com/terms-and-conditions) on Wiley Online Library for rules of use; OA articles are governed by the applicable Creative Commons License

Figure S33. The results show that the maximum energy barrier for Mg^{2+} transport is only ~0.22 eV, which is significantly lower than those of K^+ (~0.28 eV) and Ca^{2+} (~0.37 eV). This quantitative comparison directly demonstrates that Mg^{2+} experiences the lowest dehydration and migration resistance inside the channel, providing a clear mechanistic basis for the experimentally observed high Mg^{2+} selectivity over K^+ and Ca^{2+}. Furthermore, RDFs analysis revealed distinct dehydration behaviors for Mg^{2+} and K^+ (Figure S34a), and Ca^{2+} (Figure S34b) ions within the TAPA-TFP nanochannels. Mg^{2+} underwent near-complete dehydration, enabling smooth translocation through TAPA-TFP nanochannels. In contrast, K^+ experienced limited dehydration with minimal permeation, while Ca^{2+} maintained its hydration shell through water adsorption at channel interfaces, resulting in strongly hindered transport. These RDF results aligned consistently with our energy barrier (Figure S35) calculations, providing a unified microscopic view for the high Mg^{2+} selectivity. Collectively, our results demonstrated a significantly lower transport energy barrier for Mg^{2+} compared to K^+ and Ca^{2+}. This selectivity arose from the synergistic combination of TAPA-TFP's structural features, including its optimal pore dimensions, the strategically positioned O/N coordination sites within the β-ketoenamine framework, and the C═O···H—O—H hydrogen-bond network. These elements cooperatively facilitated efficient Mg^{2+} migration while effectively suppressing competing cation transport, thereby achieving exceptional Mg^{2+} selectivity and permeability.

In summary, the high Mg^{2+} selectivity of the TAPA-TFP COF arose from the synergistic effects of electrostatic interactions, coordination interactions, hydrogen bonding, and pore architecture. First, the TAPA-TFP membrane carried a higher negative surface charge, which facilitated the adsorption of Mg^{2+} onto the surfaces of the nanoscale channels. In addition, the oxygen and nitrogen atoms in the β-ketoenamine linkages provided binding sites for Mg^{2+}, and an extended hydrogen-bond network was formed between the C = O groups and water molecules, which aided in the partial dehydration of Mg^{2+}, lowered the migration energy barrier, and promoted transmembrane transport. The slightly larger pore size of TAPA-TFP further reduced the energy barrier for Mg^{2+} entering the channels. In contrast, TAPA-TFB exhibited a much lower negative surface charge, resulting in significantly reduced attraction for Mg^{2+}, combined with the absence of a hydrogen-bond network and smaller pore dimensions, further slowed Mg^{2+} transport. Overall, Mg^{2+} selectivity in TAPA-TFP emerged from the coupled effects of nanoconfinement and framework chemistry.

2.4 | Efficient Osmotic Power Conversion of TAPA-TFP Membranes

Leveraging the exceptional ion permeability and selectivity of TAPA-TFP membranes, we further investigated their osmotic power harvesting performance in the $MgCl_2$ gradient system. The low concentration solution was 0.01 M $MgCl_2$, and the high concentration solution was 0.5 M $MgCl_2$ (Figure 3a). Figure S17a presented a typical *I–V* curve of a TAPA-TFP membrane recorded in the 50-fold $MgCl_2$ salinity gradient. A high Vos of 48 mV a moderate Ios of 3.8 μA was generated. Despite the moderate Ios, a large current density of up to 5080 A m^{-2} was achieved. The ultrathin thickness of the TAPA-TFP COF channels combined with the β-ketoenamine linkages conferred ion transport properties far exceeding those of thicker COF films and conventional membranes [21, 39, 41–43]. The harvested osmotic power was calculated in a circuit with an external resistor by $P = I^2R_L$, where I was the current and R_L was the external load resistance. The maximum output power density of TAPA-TFP COF was up to 243.9 W m^{-2} at an optimal external load resistance of 12.6 kΩ (Figure 3b). Considering practical application conditions, membrane performance was evaluated across varying salinity gradients. As the $MgCl_2$ salinity gradient increased from 5-fold to 500-fold, the TAPA-TFP membrane's maximum power density rose from 8.01 to 636.6 W m^{-2}, the current density increased from 400 to 9213.3 A m^{-2}, surpassing most advanced membrane materials reported to date (Figure 3b–e and Figures S36 and S37) [21, 39, 41–43]. Calculated based on t_+ values, energy conversion efficiencies (η) of the TAPA-TFP membrane at corresponding salinity gradients were 46.1%, 46%, and 38.7%, respectively (Figure 3f).

To further investigate the transport behavior of Mg^{2+} in the nanochannel of different COF membranes, comparative *I–V* measurements were conducted using TAPA-TFB membranes with the same effective area. Unfortunately, under a 50-fold $MgCl_2$ salinity gradient, the TAPA-TFB membrane exhibited a t_+ of only 0.72, with corresponding power density and current density of 96 W m^{-2} and 4800 A m^{-2}, respectively, far lower than the osmotic power performance of the TAPA-TFP membrane (Figure 2c and Figures S38 and S39). Similarly, under 5-fold and 500-fold $MgCl_2$ salinity gradients, the t_+, power density, and current density calculated for TAPA-TFB were all significantly lower than the corresponding values for TAPA-TFP (Figure 2c and Figures S38–S42). This pronounced difference was primarily attributed to the synergistic effects of electrostatic interactions, coordination interactions, hydrogen bonding, and pore architecture in the TAPA-TFP membrane. The TAPA-TFP membrane carried a more negative surface charge, facilitating Mg^{2+} adsorption onto the nanochannel surfaces. In addition, the oxygen and nitrogen atoms in the β-ketoenamine linkages provided binding sites for Mg^{2+}, an extended hydrogen-bond network was established through C = O groups and H_2O, which assisted the partial dehydration of Mg^{2+}, lowered the migration barrier, and promoted Mg^{2+} ion transport. The slightly larger pore size of TAPA-TFP further reduced the energy barrier for Mg^{2+} entering the channels. By contrast, TAPA-TFB exhibited a much lower negative surface charge. As a result, its affinity for Mg^{2+} was significantly reduced, and the absence of a hydrogen-bonding network, combined with smaller pore dimensions, further slowed Mg^{2+} transport.

To evaluate the operational stability of the TAPA-TFP nanochannels, osmotic potential, power density, and current density were monitored over a period of 35 days. Long-term stability testing revealed no significant degradation in membrane performance after 35 days of continuous power generation under a 50-fold $MgCl_2$ salinity gradient, demonstrating exceptional operational stability (Figure 3g). Figure 3h summarizes our osmotic power generation performance and compares it with the latest reported results in terms of membrane thickness, t_+, power density, current density, energy conversion efficiency (η), and stability (Table S2). The results indicated that TAPA-TFP membranes not only exhibit ultrathin thickness and outstanding Mg^{2+} selectivity but also

16136829, 2026, 44, Downloaded from https://onlinelibrary.wiley.com/doi/10.1002/smll.74164 by Cas-Beijing Institution Of, Wiley Online Library on [09/08/2026]. See the Terms and Conditions (https://onlinelibrary.wiley.com/terms-and-conditions) on Wiley Online Library for rules of use; OA articles are governed by the applicable Creative Commons License

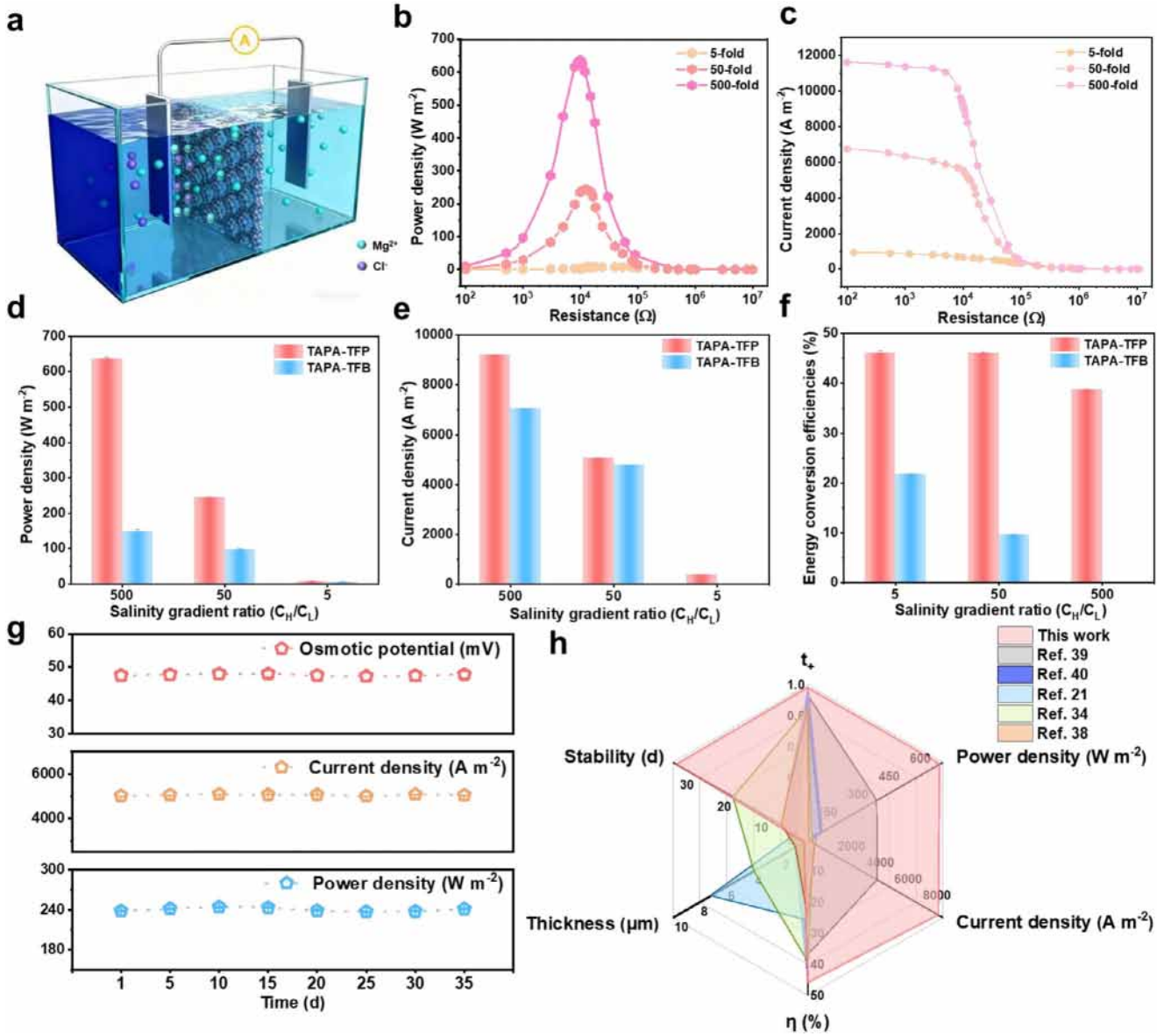


FIGURE 3 | The osmotic power conversion of the membranes. (a) Schematic representation of the experimental set-up used for osmotic power conversion. (b) Power densities of TAPA-TFP membranes in different $MgCl_2$ salinity gradients, including 5-fold, 50-fold, and 500-fold. (c) Current densities of TAPA-TFP membranes in different $MgCl_2$ salinity gradients, including 5-fold, 50-fold, and 500-fold. (d) Power densities of TAPA-TFP and TAPA-TFB membranes in different $MgCl_2$ salinity gradients, including 5-fold, 50-fold, and 500-fold. (e) Current densities of TAPA-TFP and TAPA-TFB membranes in different $MgCl_2$ salinity gradients, including 5-fold, 50-fold, and 500-fold. (f) Energy conversion efficiencies of TAPA-TFP and TAPA-TFB membranes in different $MgCl_2$ salinity gradients, including 0.05 M/0.01 M $MgCl_2$, 0.5 M/0.01 M $MgCl_2$ and 5 M/0.05 M $MgCl_2$. (g) The long-term stability plots of osmotic potentials, power densities and current densities for the TAPA-TFP membrane in a 0.5 M/0.01 M $MgCl_2$ salinity gradient. (h) Comparison of osmotic power performances of the TAPA-TFP membrane with state-of-the-art osmotic membranes.

achieve unprecedentedly high power density and current density, and superior operational stability. Furthermore, the membrane demonstrated excellent acid and alkali tolerance, maintaining structural integrity after one month of immersion in both strongly acidic (pH 2, HCl) and strongly alkaline (pH = 12, NaOH) environments (Figure S43). This remarkable chemical stability could be attributed to the chemical structure of TAPA-TFP. During the synthesis, the β-ketoenamine linkages underwent irreversible tautomerization to form a fully conjugated network, enhancing the structural robustness of the membrane and endowing it with exceptional chemical corrosion resistance.

2.5 | Iontronic Transistor and its Logic Control

Conventional electronic transistors achieve logic operations and high-density computation through current modulation across source, drain, and gate terminals (Figure 4a) [44]. However, their energy efficiency remains markedly lower than that of biological systems, particularly under low-power conditions were achieving both high-speed computation and multistate logic is inherently challenging. Each switching event relies on external electric fields to drive carrier transport and dissipates energy above the picojoule scale, fundamentally constraining their applicability in

16136829, 2026, 44, Downloaded from https://onlinelibrary.wiley.com/doi/10.1002/smll.74164 by Cas-Beijing Institution Of, Wiley Online Library on [09/08/2026]. See the Terms and Conditions (https://onlinelibrary.wiley.com/terms-and-conditions) on Wiley Online Library for rules of use; OA articles are governed by the applicable Creative Commons License

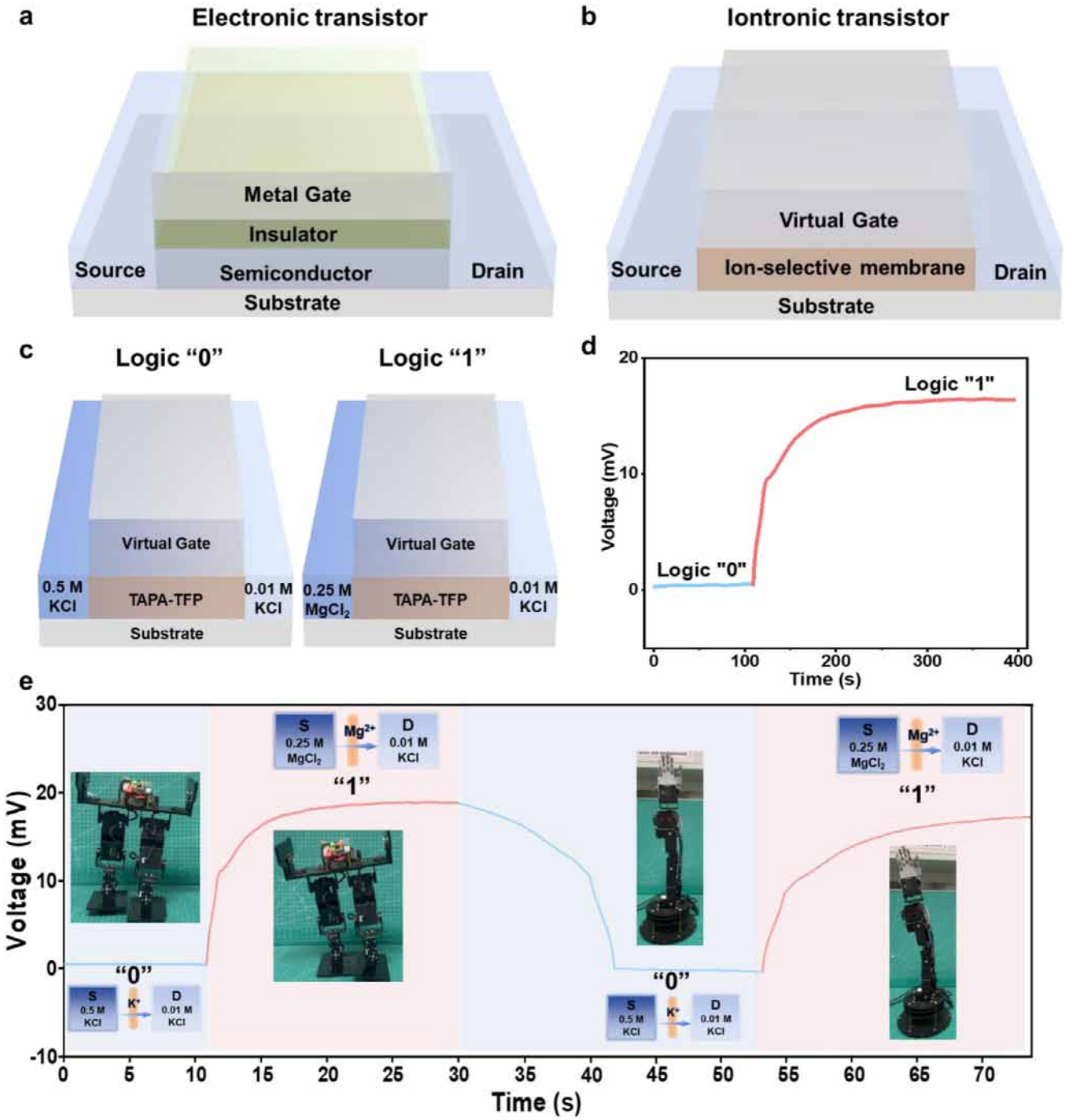


FIGURE 4 | Iontronic logic control of TAPA-TFP iontronic transistor. (a) An electronic transistor with electrons as carriers in the core of electronic devices in the information age. (b) The iontronic transistor with ions as charge carriers has virtual gates. (c) Define low and high voltage levels as 0 and 1, achieved through K^+ and Mg^{2+} ions transport. (d) Voltage signal switches when a stimulus was applied (ions). (e) Information transmission in human-machine interaction based on biomimetic ion flow of TAPA-TFP iontronic transistor.

bioinspired or biocompatible environments [45, 46]. In contrast, the TAPA-TFP membrane exhibits exceptionally high energy conversion efficiency together with intelligent regulatory behavior reminiscent of biological ion channels, representing a notable advance in both ionic logic processing and energy transduction. In living systems, Mg^{2+} channels precisely regulate transmembrane magnesium transport, maintain cellular homeostasis, and integrate ionic signals through cooperative interactions with other species. Operating without external voltage gating, these channels exploit salinity gradients, ion selectivity, and finely tuned spatial structures to achieve intrinsic "on-off" regulation of ion flow (Figure 4b) [3]. This mechanism offers fundamental insight into biological information processing and defines a framework for passive, low-energy iontronic logic. Inspired by this principle, iontronic transistors and logic architectures harness ionic gradients and selective channels to govern information flow and energy transduction, establishing a biomimetic paradigm for efficient, adaptive computation.

16136829, 2026, 44, Downloaded from https://onlinelibrary.wiley.com/doi/10.1002/smll.74164 by Cas-Beijing Institution Of, Wiley Online Library on [09/08/2026]. See the Terms and Conditions (https://onlinelibrary.wiley.com/terms-and-conditions) on Wiley Online Library for rules of use; OA articles are governed by the applicable Creative Commons License

Building upon this foundation, we designed an iontronic transistor based on TAPA-TFP nanopores that operated without an external gate voltage. Here, we introduce the concept of a "virtual gate", analogous to the gate electrode in a conventional transistor, the ionic concentration gradient between the source and drain acts as an effective control element to regulate transmembrane ion transport, enabling precise control of ion transport and logic output. A concentration difference drives the net diffusion of ions, the nanopore exhibited pronounced selectivity toward Mg^{2+} ions, directly translating the salinity gradient into a measurable transmembrane voltage and current. The β-ketoenamine structure and its tunable hydrogen-bonding network facilitated preferential Mg^{2+} migration and effectively suppressed K^+ passage. This structure allowed for controlled ionic flux in the absence of applied voltage. By exploiting ion-specific signaling arising from multivalent ion transport, the iontronic transistor achieves gate-free, energy-efficient modulation of ionic flux, defining a new paradigm for ultra-low-power logic operation and programmable information processing that emulates biological ion channels. To achieve autonomous iontronic control, a fully enclosed fluidic platform integrating programmable syringes was developed for automated solution exchange on both sides of the TAPA-TFP membrane (Figures S44 and S45). When the source and drain contained 0.01 and 0.5 M KCl, respectively, the transmembrane voltage and current stabilized at a low plateau ($\leq$ 1 mV), corresponding to a logic-low state ("0") (Figure 4c,d and Figure S46). Conversely, replacing KCl with 0.01 and 0.25 M $MgCl_2$ maintained the voltage and current at a high plateau ($\geq$ 10 mV), corresponding to a logic-high state ("1") (Figure 4c,d and Figure S46), enabling rapid and reversible switching driven by distinct ionic environments. The exceptional Mg^{2+} selectivity of the TAPA-TFP membrane is directly responsible for the distinct logic outputs. With a high Mg^{2+} transference number ($t^+ = 0.98$), the membrane strongly favors Mg^{2+} transport. When the system is exposed to KCl electrolytes, this selectivity effectively suppresses K^+ permeation, leading to a negligible transmembrane potential (logic "0" state). In contrast, when $MgCl_2$ is used, the membrane's preferential Mg^{2+} transport generates a large and stable osmotic voltage under the same salinity gradient, corresponding to the logic "1" state. This ion-specific response creates a large, consistent difference between the two states, which is critical for reliable, noise-resistant logic operation. By defining voltage thresholds, these plateau levels can be quantitatively mapped to logical outputs, constructing a programmable multivalent iontronic logic system that unifies energy and information transmission. These logical states not only serve as digital signals but also can directly actuate microelectromechanical devices. In a micro-robot demonstration, logic-low state ("0") induced left leg lifting, while the logic-high state ("1") triggered right leg lifting (Figure 4e and Video S8), enabling real-time ionic control that mimics the neuromuscular regulation of biological organisms. Together, these findings establish a unified energy-information flow paradigm, in which the high Mg^{2+} selectivity of the TAPA-TFP membrane underpins efficient osmotic power conversion while simultaneously encoding and transmitting information, illustrating the intrinsic coupling between ionic energy generation and logical operation in bioinspired iontronic systems.

TAPA-TFP nanopores enable controllable ion transport and logic output without external voltage by harnessing highly selective Mg^{2+} migration, thereby establishing a programmable multivalent-ion logic system. The β-ketoenamine framework, with its tunable hydrogen-bonding network, not only facilitated preferential Mg^{2+} transport while suppressing K^+ passage but also intrinsically coupled information transmission with energy conversion. This integrated system can directly actuate microelectromechanical devices, such as microrobots and robotic hands (Figure 4e and Videos S8 and S9), enabling rapid, biomimetic responded that emulate biological ion-channel regulation. These results underscored the potential of highly selective ion channels as bioinspired platforms for energy-information coupling. Moreover, TAPA-TFP nanopores and analogous ion-selective channels provide design principles for low-energy, passively driven iontronic logic devices, offering new avenues toward iontronic integration. In power generation and information processing, such materials can simultaneously achieve efficient osmotic power generation and logic computation, opening pathways to self-powered microsystems, wearable sensors, and adaptive biointerfaces. With further optimization of molecular architectures, channel dimensions, and multivalent-ion cooperativity, these systems could enable higher-precision logic control, multistate encoding, and complex computational operations, advancing the frontiers of iontronic logic in smart materials, artificial neural networks, and soft robotics. When integrated with microfluidics and nanoscale electronics, such architectures may ultimately yield fully autonomous microsystems that unify power generation, information processing, and actuation, realizing truly bioinspired intelligent iontronics [47–49].

3 | Discussion

In summary, we successfully synthesized a flexible, self-standing, and ultrathin β-ketoenamine COF membrane (TAPA-TFP) through an interfacial polymerization strategy. Experimental results and molecular dynamics simulations confirmed that the membrane exhibited exceptional selectivity and permeability toward Mg^{2+} ions. The key to its performance lay in the β-ketoenamine structural unit serving as binding sites for Mg^{2+} ions migration. An extended hydrogen-bond network was established through C = O groups and H_2O, which assisted the partial dehydration of Mg^{2+}, lowered the migration barrier, and promoted Mg^{2+} ions transport, resulting in a near-ideal cation transference number ($t_+ = 0.98$). The TAPA-TFP membrane were applied in osmotic power conversion, achieving a record-high power density of 636.64 W m^{-2} under a 500-fold salinity gradient, while maintaining outstanding long-term stability and pH tolerance. A key advantage of the resulting membrane was its ultrathin, large-area processability, together with exceptionally high selectivity toward Mg^{2+} ions transport, making it well-suited for emerging iontronic applications. Mg^{2+} selective channels enable iontronic logic encoding, integrating ion transport with programmable information processing and mechanical actuation, thereby advancing TAPA-TFP membranes from conventional separation materials to multifunctional iontronic platforms. The molecular design principle proposed in this work not only provides a viable pathway for constructing other multivalent ion-selective membranes but also establishes a novel paradigm through ion-specific signals generated by multi-ion transport in ion transistors, enabling gate-free regulation of ionic flux. This approach points the way forward in fields such

16136829, 2026, 44, Downloaded from https://onlinelibrary.wiley.com/doi/10.1002/smll.74164 by Cas-Beijing Institution Of, Wiley Online Library on [09/08/2026]. See the Terms and Conditions (https://onlinelibrary.wiley.com/terms-and-conditions) on Wiley Online Library for rules of use; OA articles are governed by the applicable Creative Commons License

as powering soft microrobots, sustainable power generation, magnesium batteries, seawater desalination, and brain-inspired information technologies.

4 | Experimental Section

4.1 | Preparation of Self-Standing COF Membranes

Self-standing COF membranes were successfully synthesized via interfacial polymerization (IP) at room temperature using TAPA and TFP (or TFB) as monomers [34]. In a typical procedure, 0.6 mmol of the amine monomer TAPA and 0.6 mmol of the aldehyde monomer TFP (or TFB) were dissolved in 100 mL of dichloromethane (DCM) to form the organic phase. The resulting solution was transferred into a Petri dish with a diameter of 12 cm and allowed to stand until the surface stabilized. Pure water was then carefully overlaid to form the aqueous phase, establishing a stable organic/aqueous interface. Subsequently, 1.2 mL of acetic acid solution (3.0 M) was gently added dropwise into the aqueous phase as a catalyst. The Petri dish was sealed to maintain system stability. After standing for 24 h at room temperature, a transparent and smooth membrane was clearly observed at the liquid–liquid interface. The as-formed self-standing COF membrane was collected and sequentially washed with acetone and deionized water to remove residual monomers, solvent, and catalyst, and then stored in deionized water for further characterization.

4.2 | Electrochemical Cell for Transmembrane Ion Transport

TAPA-TFP or TAPA-TFB membrane samples were typically mounted between two electrolyte cells, each containing 180 μL of electrolyte solution and equipped with a pair of Ag/AgCl reference electrodes. Ionic conductivity was measured using an electrochemical workstation (Multi Auto-lab M204) with $MgCl_2$ solutions spanning concentrations from 10^{-6} to 1 M. The voltage range was set between −1 and 1 V with a scanning step of 0.002 V. The formula for calculating ionic conductance (G) is as follows:

$$G = \left(\frac{I}{V}\right)$$

where G represents ion conductance, I denotes current (A), V signifies voltage (V).

Subsequently, to evaluate cation selectivity and ion permeability, $MgCl_2$ salinity gradients were established across the membranes, and current–voltage (I–V) curves were recorded under each gradient. The diffusion current (Ios) was determined from the I–V intercept at zero voltage, while the diffusion potential (Vos) was obtained from the intercept at zero current. For basic output performance tests of the TAPA-TFP ion transistor, a programmable electrometer (Keithley 6514) directly coupled with a synchronous data acquisition card (National Instruments 6346) was employed to record current signals. To quantify cation selectivity, the ion transference number (t_+) was used, which can be calculated using the following equations:

$$t_+ = \frac{1}{2}\left(\frac{V_{OS}}{\frac{RT}{zF} ln \frac{\gamma_{C_H} C_H}{\gamma_{C_L} C_L}} + 1\right)$$

where, Vos represents the osmotic voltage, and R, T, z, F, γ, C_H, and C_L denote the ideal gas constant, temperature, ion valence, Faraday constant, ion activity coefficient, and the ion concentrations in the high- and low-concentration solutions, respectively. For cation-selective membranes, the t_+ parameter ranges from 0 to 1, where 0 indicates no selectivity and 1 corresponds to ideal cation selectivity.

4.3 | Estimation of Osmotic Energy Conversion of TAPA-TFP

The TAPA-TFP membrane was mounted between two electrolyte cells and tested in $MgCl_2$ solutions of varying concentrations. The effective energy conversion area (S) of the membrane was approximately 7.5×10^{-10} m^2 [43]. This small, well-defined area was chosen to evaluate the intrinsic ion transport and energy conversion performance of defect-free membrane regions, minimizing interference from edge leakage, macroscopic heterogeneities, or rare defects that may mask the fundamental material performance. Under identical experimental conditions, osmotic energy conversion was evaluated across $MgCl_2$ salinity gradients of 0.01 M/0.05 M, 0.01 M/0.5 M, and 0.01 M/5 M. The external load resistance (R) was varied using a resistance box, and the corresponding current (I) was recorded. The collected osmotic power density was calculated as $P = I^2R/S$.

4.4 | Molecular Dynamics (MD) Simulation

Molecular dynamics (MD) simulations were performed to quantify the permeation rates of Mg^{2+}, Ca^{2+}, and K^+ ions through TAPA-TFP and TAPA-TFB membranes under a salinity gradient in their respective chloride solutions. Ion diffusion coefficients were calculated from the slope of the time-averaged mean square displacement (MSD) using the Einstein relation. All the MD simulations were conducted using the open-source software Large-scale Atomic/Molecular Massively Parallel Simulator (LAMMPS) [50]. Interatomic interactions between COF molecules and ions were described by the Universal Force Field (UFF) [51], while water molecules were modelled using the TIP4P potential [52]. The SHAKE algorithm [53, 54] was applied to constrain hydrogen bonds and angles in water molecules.

Periodic boundary conditions were applied in the two horizontal directions parallel to the COF membrane. To simulate the ionic transport inside the COF, a fixed boundary condition was set in the vertical direction, aligned with the COF nanochannels. Furthermore, two rigid walls were placed at the system boundaries to prevent molecule escape (Figure S23). All the simulations were performed with a time step of 1 fs.

The system was first relaxed at 300 K using the canonical ensemble (NVT) for 100 ps, and then we applied a small driven

16136829, 2026, 44, Downloaded from https://onlinelibrary.wiley.com/doi/10.1002/smll.74164 by Cas-Beijing Institution Of, Wiley Online Library on [09/08/2026]. See the Terms and Conditions (https://onlinelibrary.wiley.com/terms-and-conditions) on Wiley Online Library for rules of use; OA articles are governed by the applicable Creative Commons License

force (0.00344 eV/Å in the vertical direction) to both cations (Mg^{2+}, Ca^{2+}, and K^{+}) and anions (Cl^{-}) to accelerate the ionic transmission. It is noted that the ions' temperatures were still maintained at 300 K using the NVT ensemble [55, 56]. To calculate the MSD of ions within the COF nanochannel, we eliminated the two fixed walls and the reservoirs used for generating the salinity gradient. Periodical boundary conditions were used for all the dimensions. We first randomly added the ions and water molecules inside the COF nanochannel and then relaxed the system at 300 K for 100 ps using the NVT ensemble. Another 2 ns MD simulation with the NVT ensemble was further conducted, during which the system configurations were dumped every 20 fs. Correspondingly, MSD of ion and water molecules were calculated using these MD trajectories.

Author Contributions

D.W. and Z.W. proposed the idea and the project. D.W., Y.Z., and Z.W. supervised the whole project. D.W. and L.Y. designed all the experiments. L.Y., F.Y., Y.D. carried out the experiments in this paper. L.Y., Y.X., D.W., and Z.W. wrote the manuscript. D.W., L.Y., and Y.X. analyzed the corresponding data. Y.X. and L.Y. performed MD simulations. All authors contributed to the preparation of the manuscript.

Acknowledgements

We acknowledge financial support from the National Natural Science Foundation (grant numbers 22479016, U24A20505, and 52473205).

Conflicts of Interest

The authors declare no conflicts of interest.

Data Availability Statement

Research data are not shared.

References

1. X. Li, S. Li, X. Guo, et al., "Triboiontronics for Efficient Energy and Information Flow," *Matter* 6 (2023): 3912–3926, https://doi.org/10.1016/j.matt.2023.08.022.

2. P. Peng, F. Yang, X. Li, S. Li, Z. Wang, and D. Wei, "High-Power Iontronics Enabled by Nanoconfined Ion Dynamics," *Cell Reports Physical Science* 5 (2024): 101824, https://doi.org/10.1016/j.xcrp.2024.101824.

3. H. Qian, H. Fan, P. Peng, et al., "Biomimetic Janus MXene Membrane with Bidirectional Ion Permselectivity for Enhanced Osmotic Effects and Iontronic Logic Control," *Science Advances* 11 (2025): adx1184, https://doi.org/10.1126/sciadv.adx1184.

4. L. Yang, Z. Wang, Z. L. Wang, and D. Wei, "Porous Organic Framework Membranes with Nanostructures for Osmotic Power Conversion, Water Desalination, and Selective Separation," *ChemNanoMat* 11 (2025): 202400629, https://doi.org/10.1002/cnma.202400629.

5. J. Gao, Y. Feng, W. Guo, and L. Jiang, "Nanofluidics in Two-Dimensional Layered Materials: Inspirations from Nature," *Chemical Society Reviews* 46 (2017): 5400–5424, https://doi.org/10.1039/C7CS00369B.

6. J. Shen, G. Liu, Y. Han, and W. Jin, "Artificial Channels for Confined Mass Transport at the Sub-nanometre Scale," *Nature Reviews Materials* 6 (2021): 294–312, https://doi.org/10.1038/s41578-020-00268-7.

7. D. Lei, Y. Wang, Q. Zhang, S. Wang, L. Jiang, and Z. Zhang, "High-Performance Solid-State Proton Gating Membranes Based on Two-Dimensional Hydrogen-Bonded Organic Framework Composites," *Nature Communications* 16 (2025): 754, https://doi.org/10.1038/s41467-025-56228-8.

8. H. Zhang, X. Li, J. Hou, L. Jiang, and H. Wang, "Angstrom-Scale Ion Channels towards Single-Ion Selectivity," *Chemical Society Reviews* 51 (2022): 2224–2254, https://doi.org/10.1039/D1CS00582K.

9. Y. Zheng, Z. Zhang, T. Yin, et al., "Micron-Sized H_2MoO_3/PANI for Superfast Proton Batteries in Frozen Electrolyte through Grotthuss Mechanism," *Science Bulletin* 68 (2023): 2945–2953, https://doi.org/10.1016/j.scib.2023.11.006.

10. Y. Qian, Y. Wu, S. Qiu, et al., "A Bioinspired Free-Standing 2D Crown-Ether-Based Polyimine Membrane for Selective Proton Transport," *Angewandte Chemie International Edition* 62 (2023): 202300167, https://doi.org/10.1002/anie.202300167.

11. A. S. A. Naderi and R. F. Reilly, "Hereditary Etiologies of Hypomagnesemia," *Nature Clinical Practice Nephrology* 4 (2008): 80–89, https://doi.org/10.1038/ncpneph0680.

12. M. Hu, G. Li, K. Chen, X. Zhou, and C. Li, "A Gradient Structured SEI Enabling Record-High Areal Capacity Anode for High-Rate Mg Metal Batteries," *Chemical Engineering Journal* 480 (2024): 148193, https://doi.org/10.1016/j.cej.2023.148193.

13. A. Tomita, M. Zhang, F. Jin, et al., "ATP-Dependent Modulation of MgtE in Mg^{2+} Homeostasis," *Nature Communications* 8 (2017): 148, https://doi.org/10.1038/s41467-017-00082-w.

14. Q. Wang, H. Li, R. Zhang, et al., "Oxygen Vacancies Boosted Fast Mg^{2+} Migration in Solids at Room Temperature," *Energy Storage Materials* 51 (2022): 630–637, https://doi.org/10.1016/j.ensm.2022.07.012.

15. F. Chen, K. Huang, H.-Y. Li, et al., "Interlayer Cationic Defect Engineering in Lamellar Vanadate Cathodes Enables Ultralong-Lifespan Magnesium-Ion Batteries," *ACS Energy Letters* 10 (2025): 2052–2060, https://doi.org/10.1021/acsenergylett.5c00380.

16. J. Meng, M. Yin, K. Guo, X. Zhou, and Z. Xue, "In Situ Polymerization in COF Boosts Li-Ion Conduction in Solid Polymer Electrolytes for Li Metal Batteries," *Nano-Micro Letters* 17 (2025): 248, https://doi.org/10.1007/s40820-025-01768-3.

17. J. Li, X. Jing, Q. Li, et al., "Bulk COFs and COF Nanosheets for Electrochemical Energy Storage and Conversion," *Chemical Society Reviews* 49 (2020): 3565–3604, https://doi.org/10.1039/D0CS00017E.

18. H. Zhang, Y. Geng, J. Huang, Z. Wang, K. Du, and H. Li, "Charge and Mass Transport Mechanisms in Two-Dimensional Covalent Organic Frameworks (2D COFs) for Electrochemical Energy Storage Devices," *Energy & Environmental Science* 16 (2023): 889–951, https://doi.org/10.1039/D2EE02742A.

19. L. Samineni and M. Kumar, "Harnessing Blue Energy with COF Membranes," *Nature Nanotechnology* 17 (2022): 564–566, https://doi.org/10.1038/s41565-022-01118-z.

20. M. Wang, T. Y. Ma, Z. H. Wu, et al., "Construction of Local-Ion Trap in Phase-Reversed Mixed Matrix COF Membranes for Ultrahigh Ion Selectivity," *Angewandte Chemie International Edition* 64 (2025): 202504990, https://doi.org/10.1002/anie.202504990.

21. Z. Man, J. Safaei, Z. Zhang, et al., "Serosa-Mimetic Nanoarchitecture Membranes for Highly Efficient Osmotic Energy Generation," *Journal of the American Chemical Society* 143 (2021): 16206–16216, https://doi.org/10.1021/jacs.1c07392.

22. Q. Guo, Z. Xing, H. Guo, et al., "Creating Sodium Ion Channels via De Novo Encapsulation of Ionophores for Enhanced Water Energy Harvesting," *Advanced Materials* 37 (2025): 2420636, https://doi.org/10.1002/adma.202420636.

23. Z. Lai, Y. Ai, W. Xian, et al., "Covalent–Organic-Framework Membrane with Aligned Dipole Moieties for Biomimetic Regulable Ion Transport," *Advanced Functional Materials* 34 (2024): 2409356, https://doi.org/10.1002/adfm.202409356.

24. S. Yin, J. Li, Z. Lai, et al., "Giant Gateable Thermoelectric Conversion by Tuning the Ion Linkage Interactions in Covalent Organic Framework

16136829, 2026, 44, Downloaded from https://onlinelibrary.wiley.com/doi/10.1002/smll.74164 by Cas-Beijing Institution Of, Wiley Online Library on [09/08/2026]. See the Terms and Conditions (https://onlinelibrary.wiley.com/terms-and-conditions) on Wiley Online Library for rules of use; OA articles are governed by the applicable Creative Commons License

Membranes," *Nature Communications* 15 (2024): 8137, https://doi.org/10.1038/s41467-024-52487-z.

25. W. Meng, S. Chen, Z. Guo, et al., "Three-Dimensional Cationic Covalent Organic Framework Membranes for Rapid and Selective Lithium Extraction from Saline Water," *Nature Water* 3 (2025): 191–200, https://doi.org/10.1038/s44221-024-00379-3.

26. S. Bao, Z. Ma, L. Yu, et al., "Randomly Oriented Covalent Organic Framework Membrane for Selective Li^+ Sieving from Other Ions," *Nature Communications* 16 (2025): 3896, https://doi.org/10.1038/s41467-025-59188-1.

27. G. Wang, L. Shao, and S. Zhang, "Membrane-Ion Interactions Creating Dual-Nanoconfined Channels for Superior Mixed Ion Separations," *Advanced Materials* 37 (2025): 2414898, https://doi.org/10.1002/adma.202414898.

28. Y. Shen, Y. Wang, Y. Miao, Q. Li, X. Zhao, and X. Shen, "Anion-Incorporated Mg-Ion Solvation Modulation Enables Fast Magnesium Storage Kinetics of Conversion-Type Cathode Materials," *Advanced Materials* 35 (2023): 2208289, https://doi.org/10.1002/adma.202208289.

29. E. Pousaneh, T. Rüffer, K. Assim, et al., "Magnesium β-ketoiminates as CVD Precursors for MgO Formation," *RSC Advances* 8 (2018): 19668–19678, https://doi.org/10.1039/C8RA01851K.

30. Z. Du, W. Lee, and D. Feng, "Multivalent Ion-Conducting Metal- and Covalent- Organic Frameworks," *ACS Applied Energy Materials* 8 (2025): 13040–13049, https://doi.org/10.1021/acsaem.5c01925.

31. J. L. Segura, M. J. Mancheño, and F. Zamora, "Covalent Organic Frameworks Based on Schiff-base Chemistry: Synthesis, Properties and Potential Applications," *Chemical Society Reviews* 45 (2016): 5635–5671, https://doi.org/10.1039/C5CS00878F.

32. S. Kandambeth, K. Dey, and R. Banerjee, "Covalent Organic Frameworks: Chemistry beyond the Structure," *Journal of the American Chemical Society* 141 (2019): 1807–1822, https://doi.org/10.1021/jacs.8b10334.

33. W. Tang, J. Zeng, F. Bian, H. Lin, H. Zhao, and Z.-Y. Lu, "Engineering Heteroatomic Structures in Pt Single-Atom Anchored Covalent Organic Frameworks for Enhanced Photocatalytic Hydrogen Evolution Reaction," *Journal of Materials Chemistry A* 13 (2025): 19682–19694, https://doi.org/10.1039/D5TA01922B.

34. J. Liu, G. Han, D. Zhao, et al., "Self-Standing and Flexible Covalent Organic Framework (COF) Membranes for Molecular Separation," *Science Advances* 6: abb1110, https://doi.org/10.1126/sciadv.abb1110.

35. L. Yang, L. N. Y. Cao, S. Li, et al., "MOFs/MXene Nano-Hierarchical Porous Structures for Efficient Ion Dynamics," *Nano Energy* 129 (2024): 110076, https://doi.org/10.1016/j.nanoen.2024.110076.

36. H. Qian, P. Peng, H. Fan, et al., "Horizontal Transport in $Ti_3C_2T_x$ MXene for Highly Efficient Osmotic Energy Conversion from Saline-Alkali Environments," *Angewandte Chemie International Edition* 63 (2024): 202414984, https://doi.org/10.1002/anie.202414984.

37. R. C. Rollings, A. T. Kuan, and J. A. Golovchenko, "Ion Selectivity of Graphene Nanopores," *Nature Communications* 7 (2016): 11408, https://doi.org/10.1038/ncomms11408.

38. J. Zong, W. Ma, Y. Jiang, et al., "Giant Osmotic Power Density Generation with an Anion-Selective AB-Stacking Covalent-Organic Framework Bilayer," *The Innovation* 6 (2025): 100908, https://doi.org/10.1016/j.xinn.2025.100908.

39. T. Zhu, Y. Kong, B. Lyu, et al., "3D Covalent Organic Framework Membrane with Fast and Selective Ion Transport," *Nature Communications* 14 (2023): 5926, https://doi.org/10.1038/s41467-023-41555-5.

40. L. Yang, S. Li, H. Qian, Z. Wang, Z. L. Wang, and D. Wei, "Osmotic Power Generation Based on Nanoconfined Materials," *MRS Energy & Sustainability* 11 (2024): 193–218, https://doi.org/10.1557/s43581-024-00104-3.

41. X. Lin, P. Liu, W. Xin, et al., "Heterogeneous MXene/PS-b-P2VP Nanofluidic Membranes with Controllable Ion Transport for Osmotic Energy Conversion," *Advanced Functional Materials* 31 (2021): 2105013, https://doi.org/10.1002/adfm.202105013.

42. L. Ding, M. Zheng, D. Xiao, et al., "Bioinspired $Ti_3C_2T_x$ MXene-Based Ionic Diode Membrane for High-Efficient Osmotic Energy Conversion," *Angewandte Chemie International Edition* 61 (2022): 202206152, https://doi.org/10.1002/anie.202206152.

43. W. Jiang, J. Zhou, X. Zhong, et al., "Axial Alignment of Covalent Organic Framework Membranes for Giant Osmotic Energy Harvesting," *Nature Sustainability* 8 (2025): 446–455, https://doi.org/10.1038/s41893-024-01493-6.

44. C.-Y. Lin, C. Combs, Y.-S. Su, L.-H. Yeh, and Z. S. Siwy, "Rectification of Concentration Polarization in Mesopores Leads to High Conductance Ionic Diodes and High Performance Osmotic Power," *Journal of the American Chemical Society* 141 (2019): 3691–3698, https://doi.org/10.1021/jacs.8b13497.

45. J.-P. Colinge, C.-W. Lee, A. Afzalian, et al., "Nanowire Transistors without Junctions," *Nature Nanotechnology* 5 (2010): 225–229, https://doi.org/10.1038/nnano.2010.15.

46. S. Datta, W. Chakraborty, and M. Radosavljevic, "Toward Attojoule Switching Energy in Logic Transistors," *Science* 378 (2022): 733–740, https://doi.org/10.1126/science.ade7656.

47. S. Wang, X. Chen, C. Zhao, et al., "An Organic Electrochemical Transistor for Multi-Modal Sensing, Memory and Processing," *Nature Electronics* 6 (2023): 281–291, https://doi.org/10.1038/s41928-023-00950-y.

48. Z. Zhang, L. Wen, and L. Jiang, "Nanofluidics for Osmotic Energy Conversion," *Nature Reviews Materials* 6 (2021): 622–639, https://doi.org/10.1038/s41578-021-00300-4.

49. Z. Sun, T. He, Z. Ren, et al., "Moving toward Human-like Perception and Sensation Systems—From Integrated Intelligent Systems to Decentralized Smart Devices," *SmartSys* 1 (2025): 4, https://doi.org/10.1002/sys3.4.

50. S. Yalameha, Z. Nourbakhsh, and D. Vashaee, "ElATools: A Tool for Analyzing Anisotropic Elastic Properties of the 2D and 3D Materials," *Computer Physics Communications* 271 (2022): 108195, https://doi.org/10.1016/j.cpc.2021.108195.

51. A. Marquez and J. F. Sanz, "Ab Initio CASSCF Study of the Electronic Structure of the Transition-Metal Alkylidene-Like Complexes Mo-M'H2 (M' = carbon, silicon, germanium and tin)," *Journal of the American Chemical Society* 114 (1992): 10019–10024, https://doi.org/10.1021/ja00051a039.

52. J. L. F. Abascal and C. Vega, "A General Purpose Model for the Condensed Phases of Water: TIP4P/2005," *The Journal of Chemical Physics* 123 (2005): 234505, https://doi.org/10.1063/1.2121687.

53. J. P. Ryckaert, G. Ciccotti, and H. J. C. Berendsen, "Numerical Integration of the Cartesian Equations of Motion of a System with Constraints: Molecular Dynamics of N-Alkanes," *Journal of Computational Physics* 23 (1977): 327–341, https://doi.org/10.1016/0021-9991(77)90098-5.

54. H. C. Andersen, "Rattle: A "Velocity" Version of the Shake Algorithm for Molecular Dynamics Calculations," *Journal of Computational Physics* 52 (1983): 24–34, https://doi.org/10.1016/0021-9991(83)90014-1.

55. W. Shinoda, M. Shiga, and M. Mikami, "Rapid Estimation of Elastic Constants by Molecular Dynamics Simulation under Constant Stress," *Physical Review B* 69 (2004): 134103, https://doi.org/10.1103/PhysRevB.69.134103.

16136829, 2026, 44, Downloaded from https://onlinelibrary.wiley.com/doi/10.1002/smll.74164 by Cas-Beijing Institution Of, Wiley Online Library on [09/08/2026]. See the Terms and Conditions (https://onlinelibrary.wiley.com/terms-and-conditions) on Wiley Online Library for rules of use; OA articles are governed by the applicable Creative Commons License

56. M. E. Tuckerman, J. Alejandre, R. López-Rendón, A. L. Jochim, and G. J. Martyna, "A Liouville-Operator Derived Measure-Preserving Integrator for Molecular Dynamics Simulations in the Isothermal–Isobaric Ensemble," *Journal of Physics A: Mathematical and General* 39 (2006): 5629–5651, https://doi.org/10.1088/0305-4470/39/19/S18.

Supporting Information

Additional supporting information can be found online in the Supporting Information section.

Supporting File 1: smll74164-sup-0001-SuppMat.docx.

Supporting File 2: smll74164-sup-0002-VideoS1-S9.zip.

16136829, 2026, 44, Downloaded from https://onlinelibrary.wiley.com/doi/10.1002/smll.74164 by Cas-Beijing Institution Of, Wiley Online Library on [09/08/2026]. See the Terms and Conditions (https://onlinelibrary.wiley.com/terms-and-conditions) on Wiley Online Library for rules of use; OA articles are governed by the applicable Creative Commons License